
Time varying climate derived root zone storage capacity

A method to explain the rainfall-runoff anomalies of the Meuse catchment?

By

ALESSANDRO SAVAZZI



Department of Environmental Engineering
TU DELFT

Research conducted at the Systems Analysis, Integrated Assessment and Modelling (SIAM) department of EAWAG, Switzerland.

JANUARY 2019

Supervisors:
Dr. Fabrizio Fenicia
Dr. Markus Hrachowitz
Dr.ir. Miriam Coenders

ABSTRACT

The Meuse river basin covers an area of 33,000 km², touches five countries and is a major communication route in Europe. It is one of the catchments with longest streamflow records, with daily measures of discharge dating back to the beginning of the previous century. Attempts to model streamflow with standard hydrological models revealed that average streamflow was consistently overestimated by the model in the period 1933-1968. Different attempts to explain such anomaly can be found in the literature. In this work we hypothesise that this anomaly could be resolved by considering a time varying root zone storage capacity, represented by a model parameter ($S_{u,max}$), which has affected the partitioning between precipitation and streamflow. Vegetation is in fact believed to adjust root zone storage capacity to overcome droughts with a return period of about 20 years. To test our hypothesis, a semi-distributed conceptual model, based on the FLEX modelling approach, was used. A time varying $S_{u,max}$ was obtained with two approaches: by calibration of the model parameters in a moving time window, and by derivation of $S_{u,max}$ directly from climate variables. The results show that adding time dependency to $S_{u,max}$ improves the mean flow simulation, however not to a degree that it fully explains the observed anomaly. Deriving $S_{u,max}$ directly from climate variables delivered a better fit to the average streamflow than calibration, which confirms the feasibility of a climate derived root zone storage capacity in hydrological modelling.

ABBREVIATIONS

All the fluxes have units of L/T (e.g. mm/day) while all the states have units of L .

- IR: Interception reservoir.
- UR: Unsaturated reservoir.
- FR: Fast reacting reservoir.
- SL: Slow reacting reservoir.
- LW_f : Lag function weights.
- $S_{i/u/f/s}$: Storage of the interception/unsaturated/fast/slow reservoir, respectively.
- $S_{u,max}$: Root-zone storage capacity.
- P_t : Total precipitation.
- P_u : Effective precipitation.
- P_s : Inflow to the slow reservoir.
- P_f : Inflow to the lag function.
- P_{fl} : Inflow to the fast reservoir.
- Q_t : Total discharge.
- Q_s : Outflow of the slow reservoir.
- Q_f : Outflow of the fast reservoir.
- Q_u : Percolation from UR.
- Q_q : Runoff from UR.
- Q_p : Preferential recharge.
- $E_{p,i}$: Potential evaporation from the canopy.
- E_i : Actual evaporation from the interception reservoir.
- E_{Penn} : Potential evaporation from UR according to Penaman-Monteith equation.
- $E_{p,u}$: Potential transpiration from UR.
- E_u : Actual transpiration from the unsaturated reservoir.
- $E_a = E_i + E_u$: Total actual evaporation and transpiration.

TABLE OF CONTENTS

	Page
List of Tables	vi
List of Figures	vii
1 Introduction	1
1.1 The Meuse river basin	1
1.2 Problem statement	3
1.3 Previous researches	3
1.4 Research question	4
2 Methods	5
2.1 Model description	5
2.1.1 Input data	7
2.2 Computational model	7
2.2.1 Discretization technique	7
2.3 Parameter optimisation: calibration	8
2.3.1 Objective function definition	8
2.3.2 Search algorithm	9
2.4 Experiment description	9
2.4.1 Root-zone storage capacity	10
3 Results	15
3.1 Hydrographs	20
3.2 Actual transpiration	25
4 Discussion and Remarks	29
5 Conclusions	31
A Details of the hydrological model	33
A.1 List of equations	33

A.2 Model parameters	36
Bibliography	37

LIST OF TABLES

TABLE	Page
3.1 Nash-Sutcliffe efficiency (NSE) of daily discharge for different time intervals.	16
3.2 Used values of $S_{u,max}$ (in mm).	17
3.3 Nash-Sutcliffe efficiency (NSE) of annual averaged discharge for different time intervals.	17
3.4 Performance metrics evaluated over the period 1911-2000 from daily data.	19
3.5 Performance metrics evaluated over the period 1911-2000 from annual averaged data.	19
A.1 Model equations	34
A.2 Description of the Penman-Monteith equation	35
A.3 Model parameters	36

LIST OF FIGURES

FIGURE	Page
1.1 Meuse river basin	2
1.2 Land cover changes	2
2.1 Scheme of the model	5
2.2 Logistic function	6
2.3 Daily water deficits for 1995	11
2.4 Time evolution of annual maximum water deficit	12
2.5 Gumbel distribution of maximum water deficits	13
2.6 Inverse Cumulative Distribution Function	14
3.1 Nash Sutcliffe Efficiency of daily discharge	16
3.2 1993 flood hydrograph	18
3.3 Nash Sutcliffe Efficiency of annual mean discharge	19
3.4 Hydrograph: time invariant calibrated and WB derived $S_{u,max}$	21
3.5 Hydrograph: time invariant and variant, calibrated $S_{u,max}$	22
3.6 Hydrograph: time invariant and variant, WB derived $S_{u,max}$	22
3.7 Model error for the cases of WB derived $S_{u,max}$	23
3.8 Scatter plots of modelled and observed mean annual discharge	24
3.9 Actual transpiration: time invariant and variant, calibrated $S_{u,max}$	25
3.10 Actual transpiration: time invariant and variant, WB derived $S_{u,max}$	26
3.11 Actual transpiration: comparison of different correction methods	27

INTRODUCTION

1.1 The Meuse river basin

The study area of this work is defined by the Meuse river basin (figure 1.1). The Meuse is one of the major rivers in Europe: it stretches for about 875 km (Min Tu, 2006) from the source in France to the confluence with the Rhine in the Netherlands. The catchment covers an area of 33,000 km², including parts of France, Belgium, Luxembourg, Germany and the Netherlands. The maximum elevation in the basin is over 500 m a.s.l. in the French region of the Ardennes, while elevations of less than 100 m a.s.l. can be found in the Dutch lowlands (Pfister et al., 2004). The differences in elevation strongly influence the precipitation pattern, resulting in maximum values of 1000-1300 mm/year over the Ardennes and minimum values of 700-800 mm/year in the lower areas (Min Tu, 2006). Snow plays a marginal role in the runoff generation process and the catchment can be classified as rain-fed (Kwadijk and Rotmans, 1995). Although rainfall is evenly distributed throughout the year, seasonality of the evaporation rate leads to strong variability of the discharge regime of the river. As a results, most of the floods observed in the past century occurred during winter. In the summer months floods are usually local and caused by convective storm events. (Pfister et al., 2004; Tu et al., 2004, 2005; Min Tu, 2006).

Daily records of the Meuse discharge at the gauging station of Borgharen dates back to 1911 and represents an exceptionally long data set. Over the past centuries the Meuse river basin, similarly to most of the European catchments, experienced severe alterations of land use. According to the CORINE data set, at the end of the 20th century, upstream of the Belgian-Dutch border, about 34% of the land was agricultural, 21% pasture, 36% forest and 9% urban. Although the overall coverage has remained relatively stable throughout the past 100 years, the forest type has changed significantly: the ratio between deciduous and coniferous went from 3.5 at the beginning of the 20th century to 1.118 at the end of the century. (Tu et al., 2005; Ashagrie et al.,

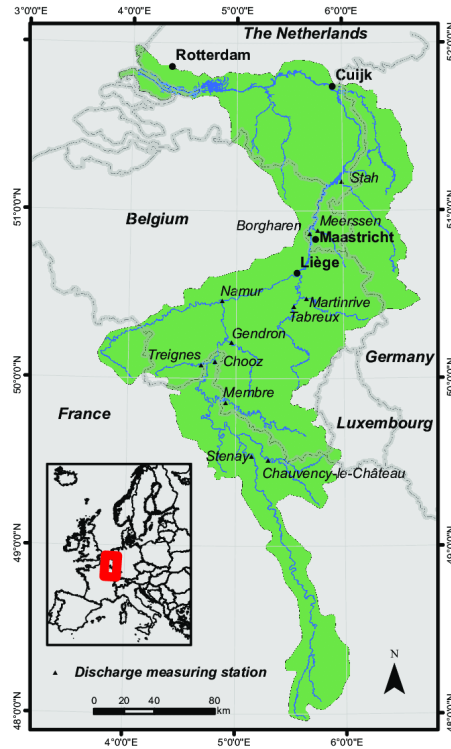


FIGURE 1.1. Meuse river basin (Ward et al., 2008).

2006). Figure 1.2 shows the relative changes of land cover over the 20th century for the five land types considered. It can be noticed that the percentage of deciduous forest went from 28% in 1911 to a minimum of 18.5% in 1974, while the percentage of coniferous forest increased from 8% in 1911 to a maximum of 17.5% in 1974.

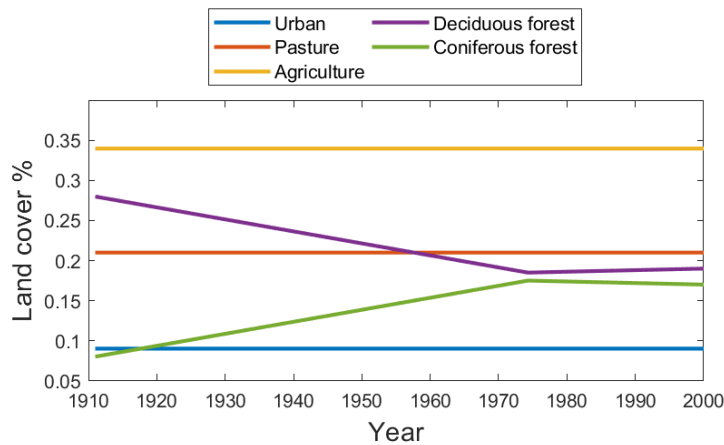


FIGURE 1.2. Changes in land cover over the 20th century.

1.2 Problem statement

According to the European Environmental Agency (EEA, 2001), floods are the most costly and common environmental disasters in Europe. Since the Meuse river basin is an important communication route, several bridges cross its stream and cities are built on the banks, accurate forecasting of the river discharge is crucial to the economy of central Europe and for the safety of the river users.

Data also suggest that the rainfall-runoff response of the catchment has changed in the past decades: five of the seven largest floods in the period 1911-2003 occurred in the last two decades (i.e. 1984, 1993, 1995, 2002 and 2003) (Tu et al., 2005). Dramatic damages caused by these floods led to a strong interest in understanding the causes (Wit et al., 2001; Min Tu, 2006; Nienhuis, 2008). Great attention was given to land use and climate changes, as they are generally recognised to be main factors affecting the behaviour of a catchment (Dale, 1997; Peel and Blöschl, 2011) and are expected to play an increasing role in the rainfall-runoff relationship everywhere in the world (De Roo et al., 2001; Wit et al., 2001; Pfister et al., 2004; Tu et al., 2005; Ward et al., 2008).

For the Meuse river, Ashagrie et al. (2006) noticed that in the 20th century, specific periods showed systematic differences in the rainfall-runoff relationship and they could not be related to land use change or to errors in the available data; an analysis of the annual and inter-annual trends of rainfall also excluded climate change to have significantly influenced precipitations patterns in this area. Later researches tried to explain why model simulation overestimated the mean annual discharge between the year 1933 and 1968. The present work can be classified among these.

1.3 Previous researches

The observed changes of flood distribution and catchment behaviour led researchers to question the current understanding of the main hydrological processes in the Meuse basin; some corrections to the state of the art hydrological model have been proposed in recent years (Fenicia et al., 2009; de Boer, 2017).

One hypothesis is that a more spatially distributed model is needed to represent the Meuse river basin. Even if promising results in considering distributed features in the Meuse catchment have been shown by de Boer (2017), the current operational forecasting system of the Meuse does not take into account spatial variability of the landscape, topography or vegetation (Bouaziz and Hrachowitz, 2017).

Another interesting research suggests that, between 1930 and 1965, forest potential evaporation was higher than in the rest of the century due to younger vegetation (Fenicia et al., 2009). By calibrating over small time intervals a parameter controlling potential transpiration (stomatal resistance coefficient), a great improvement of the model performance was achieved

in the mentioned study. Although a time dependent stomatal resistance coefficient allowed a successful fit of the observed discharge, not enough arguments about the evaporative demand of a growing forest were provided and the actual physical meaning of this time varying parameter might not be the one stated in the research. In their work Fenicia et al. (2009) used a semi-distributed conceptual hydrological model similar to the one used by Ashagrie et al. (2006) (the latter using an HBV instead of a FLEX framework). It can be argued that a parameter correcting the potential transpiration can always improve a model's performance since it directly changes one of the fluxes of the total water balance. The result is that with such time varying parameter the model has strong equifinality (many combinations of parameters can compensate for the same effect) and it becomes hard to give physical meaning to the parameters.

1.4 Research question

The aim of this work is to investigate whether the behaviour of the Meuse basin from 1911 to 2000 can be explained considering time variability of catchment characteristics which do not directly alter potential transpiration. Specifically, the role of a time varying root-zone storage capacity was studied. The hypothesis takes place from studies arguing that vegetation builds its root-zone storage capacity adapting to climate and so dynamically at time scales of climate variability. (Gao et al., 2014; Nijzink et al., 2016; de Boer-Euser et al., 2016).

This work also aims at reducing the equifinality of the state of the art conceptual model for this catchment and at improving the physical meaning of model parameters.

2.1 Model description

As mentioned in Chapter 1, this work builds up from the results of Fenicia et al. (2009). For consistency reasons the same model framework and structure was used; although the perceptual model was not questioned, some of the equations of the conceptual model were changed according to more recent literature (Fenicia et al., 2011, 2014).

The structure (figure 2.1) is of a semi-distributed conceptual model based on the FLEX modelling approach (Fenicia et al., 2007).

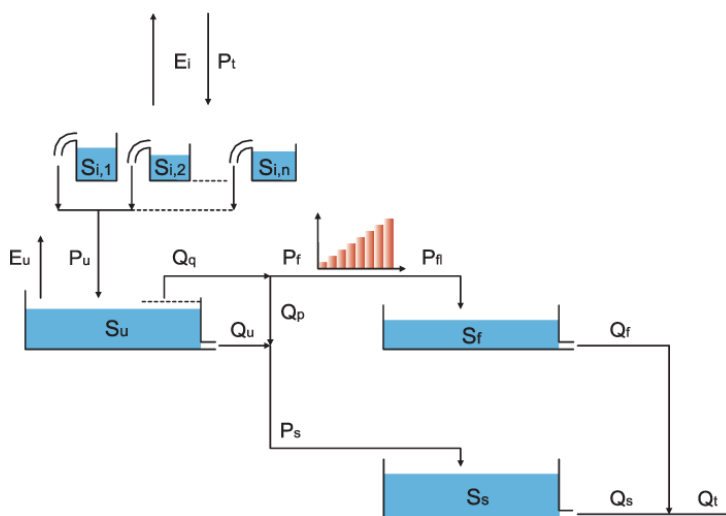


FIGURE 2.1. Schematic representation of the FLEX model used.

Evaporation (E_i) takes place from an interception reservoir (IR) comprehensive of five different land-uses: urban, pasture, agriculture, deciduous forest and coniferous forest. This reservoir feeds an unsaturated reservoir (UR) with effective precipitation (P_u); here, transpiration (E_u), runoff (Q_q) and percolation (Q_u) occur. The runoff is partitioned into a flux (P_f) which is routed to a fast reservoir (FR) through a triangular transfer function, and a second flux (preferential recharge Q_p) which, summed to the percolation, feeds a slow reacting reservoir (SR). The sum of the fast and slow discharge represents the total catchment discharge: $Q_t = Q_f + Q_s$.

The entire list of equations used to describe the processes is presented in Appendix A. Here it is important to mention that the partitioning between effective precipitation and runoff is controlled in the unsaturated reservoir by the parameter $S_{u,max}$ (root-zone storage capacity). Figure 2.2 shows, indeed, that the runoff coefficient varies with the storage in UR (S_u) according to a function (logistic curve) stretched by the parameter $S_{u,max}$ and whose steepness is controlled by another parameter (β). Defining $\bar{S}_u = \frac{S_u}{S_{u,max}}$, the equation used for the runoff is as follow:

$$(2.1) \quad Q_q = P_u f(\bar{S}_u | \beta) = P_u \frac{C_r - C_{r,min}}{C_{r,max} - C_{r,min}},$$

where C_r is the runoff coefficient:

$$(2.2) \quad C_r = \frac{1}{1 + \exp\left(\frac{-\bar{S}_u + 1/2}{\beta}\right)}.$$

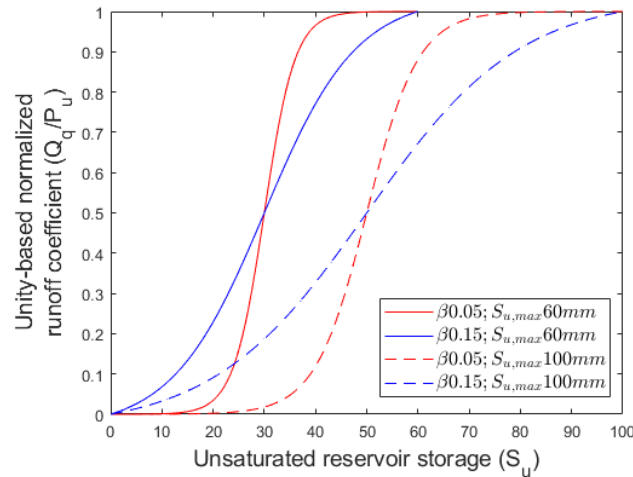


FIGURE 2.2. Constitutive function for runoff generation.

Equation 2.1 is written in such a way that the multiplying factor of P_u varies within the range [0 1].

2.1.1 Input data

The data available for this work are daily records of river discharge at Borgharen from 1911 to 2000 (www.waterbase.nl), precipitation from various rain gauges of the catchment (Ashagrie et al., 2006) and meteorological data from the station of De Bilt in the Netherlands (www.knmi.nl). With the meteorological data, the potential evaporation from the interception reservoir ($E_{p,i}$) was derived using the Penman-Monteith equation (eq. A.1) under the assumption of zero surface resistance (r_c). The differences within the land types are reflected in the values used for the aerodynamic resistance (r_a). The potential transpiration from UR was also calculated through the Penman-Monteith equation, in this case r_c varied for each land type.

Differently from what was performed by Fenicia et al. (2009), no stomatal resistance coefficient was used as a multiplying factor of r_c . This calibration parameter accounts for variation of forest transpiration with stand age by directly modifying the potential transpiration and so the water balance. As mentioned before this work wants to question the assumption that this parameter effectively represents forest age and that its ability to mimic the rainfall-runoff anomaly from 1935 to 1964 is not an artefact of the fact that it modifies the water balance.

It has to be noticed that, although the stomatal resistance coefficient must be constant in this work, the assumption of considering it equal to one might be wrong; for this reason another correcting parameter was introduced (L_e) its value was calibrated for every experiment but always kept constant over the 90 years. The role of L_e can be linked to a correction of possible systematic errors and biases in the data set.

2.2 Computational model

The conceptual model described in section 2.1 was coded using the Fortran programming language. The interception reservoir was coded independently from the rest of the model and the parameters controlling its behaviour were not calibrated but taken from the literature and kept constant throughout all experiments, as described in Appendix A.

2.2.1 Discretization technique

The same time resolution at which the input were provided have been used for the outputs: outputs are given at daily resolution. The model time step is of one day and the time stepping scheme uses an Euler implicit discretization technique.

Given the general ordinary differential equation of a reservoir (eq. 2.3)

$$(2.3) \quad \frac{dS}{dt} = \mathbf{g}(S),$$

where $\mathbf{g}(S)$ considers all the fluxes entering and leaving the reservoir; according to the first order implicit Euler scheme, the following equations holds:

$$(2.4) \quad S^{t+1} = S^t + \Delta t \mathbf{g}(S^{t+1}).$$

Although this implicit scheme is computationally costlier than its implicit counterpart (i.e. Euler explicit), it provides better reliability and efficiency as a consequence of being an unconditionally stable scheme. (Clark and Kavetski, 2010; Kavetski and Clark, 2010).

2.3 Parameter optimisation: calibration

Calibration was performed maintaining daily time intervals of the quantities involved so, the objective function was evaluated on time series with daily resolution.

2.3.1 Objective function definition

The objective function used to calibrate the model is based on the maximum-likelihood estimation (MLE). The set of model parameters to be estimated is denoted with $\boldsymbol{\theta}$. Assuming a normal distribution where we define the sample of n elements to be the vector of the distances between observed discharge and modelled discharge ($E_i = Q_{\text{obs},i} - Q_{\text{mod},i}(\boldsymbol{\theta})$), the mean to be zero ($\mu = 0$) and the standard deviation (σ) to be estimated within a range; the PDF appears to be:

$$(2.5) \quad N(E_i | \mu, \sigma) = N(Q_{\text{obs},i} - Q_{\text{mod},i} | 0, \sigma) = \frac{1}{\sqrt{2\pi\sigma^2}} \exp - \frac{(Q_{\text{obs},i} - Q_{\text{mod},i})^2}{2\sigma^2} .$$

Given the assumption that the observations from the sample (E) are independently and identically distributed (IID), the likelihood function can be written as:

$$(2.6) \quad \mathcal{L}(\boldsymbol{\theta}, \sigma; \mathbf{Q}_{\text{obs}}) = \prod_{i=1}^n N(Q_{\text{obs},i} - Q_{\text{mod},i} | 0, \sigma) = \left(\frac{1}{\sqrt{2\pi\sigma^2}} \right)^n \exp - \frac{\sum_{i=1}^n (Q_{\text{obs},i} - Q_{\text{mod},i})^2}{2\sigma^2} .$$

It is important to notice that the value of the likelihood function is influenced by the set of model parameters ($\boldsymbol{\theta}$) since Q_{mod} depends on it. Moreover for practical computational reasons the log-likelihood is taken. This results in the following function to be maximised during the calibration process.

$$(2.7) \quad \log \mathcal{L}(\boldsymbol{\theta}, \sigma; \mathbf{Q}_{\text{obs}}) = -\frac{n}{2} \log(2\pi) - \frac{n}{2} \log(\sigma^2) - \frac{1}{2\sigma^2} \sum_{i=1}^n (Q_{\text{obs},i} - Q_{\text{mod},i}(\boldsymbol{\theta}))^2 .$$

2.3.2 Search algorithm

To find the set of parameters corresponding to the maximum value of the objective function the Shuffled Complex Evolution (SCE-UA) method was used. This algorithm minimises the objective function, while the likelihood function is usually to be maximised, so a minus sign is added in front of the likelihood function. To run the model calibration, a range of possible values for each parameter was given to the search algorithm; three of the parameters (β , Kf and Ks) were calibrated in the log domain. Table A.3 includes the calibration ranges used.

As explained by Duan et al. (1993), this robust and efficient algorithm is based on four successful concepts of global optimisation: the combination of random and deterministic approaches, the concept of clustering, the systematic evolution of points spanning the space and the concept of competitive evolution. The method reduces the chances of getting trapped in local optima by using multiple complexes and periodically shuffling them (Duan et al., 1992).

The maximum number of function evaluations allowed during the optimisation was set to 10,000; the maximum number of evolution loops before convergence to 10 and the number of complexes was set to 5.

2.4 Experiment description

In order to answer the research question two sets of experiments were performed. Both were divided in two phases: first, no time dependency was given to the model parameters; in a second phase, time variability of the quantity $S_{u,max}$ was introduced.

The first phase of both the sets of experiments aimed at reproducing the results obtained by Ashagrie et al. (2006) and verify that the anomaly observed in the mid-century was correctly captured by the model used in the present work. In the second phase, one or more parameters assumed different values according to the modelled year: one set of parameter before the anomaly (1911-1934), another set of parameters during the anomaly (1935-1964) and a third set of parameters after the anomaly (1965-2000). This allowed to consider time varying characteristics of the catchment.

In the first set of experiments (calibrated root-zone storage capacity) all model parameters (see table A.3 in Appendix A) were calibrated over the entire time series (1911-2000) and then, maintaining the correction factor for transpiration (L_e) fixed to the obtained value, the model was calibrated separately for each of the three time windows (1911-1934; 1935-1964; 1965-2000). As mentioned, this second step added time variability and returned three parameter sets (one for each time window) and so three values of $S_{u,max}$. The first set of experiments allowed to give a benchmark to the maximum improvement of the objective function achievable with time varying parameters but without correcting potential transpiration over time.

For the second set of experiments (water balance derived root zone capacity), the computational model was modified so that the parameter $S_{u,max}$ was not to be calibrated; instead,

its value was fed as input after being calculated from climate data (Nijzink et al., 2016). With this approach the calibration parameters were reduced from eight to seven, although the model structure remained the same as in the calibrated root-zone storage capacity approach. As a result, the objective function was expected to reach lower values for the second set of experiments and, at time steps at which the objective function is evaluated, the modelled hydrograph was expected to deliver a worst fit compared to the first set of experiments. When adding time dependency to the model with a water balance derived root-zone storage capacity, only the parameter $S_{u,max}$ was let vary and its value was obtained for each time window from climate data. For this second phase of the second set of experiments, another calibration was performed but, as mentioned, calibration parameters were kept constant over the entire time frame (1911-2000). With this approach, it is clear that, for the second set of experiments, any change in the model performance is caused by the introduced time variability of $S_{u,max}$ and no other parameters are responsible for a correction of the anomaly.

The formulation of the two mentioned set of experiments allowed to test also the applicability to the Meuse catchment of the method proposed by Gao et al. (2014) to calculate root-zone storage capacity from climate data.

Before presenting the results in Chapter 3, Chapter 2.4.1 explains how $S_{u,max}$ was derived for the second set of experiments.

2.4.1 Root-zone storage capacity

The method used to determine values of $S_{u,max}$ from climate data was proposed by Gao et al. (2014) and successfully tested in successive works (Nijzink et al., 2016; de Boer-Euser et al., 2016). The calculation is based on the idea that vegetation builds its root system in the most efficient way: maximise water accessibility and minimise the waste of resources. According to Gao et al. (2014), this corresponds to growing roots that allow access to enough water to survive a drought with a return period of around 20 years. It is then possible to calculate the value of this drought and use it as maximum root-zone storage capacity of the catchment (Gao et al., 2014). In this work a Gumbel distribution (Gumbel, 1941) was fitted to the maxima annual water deficits to determine $S_{u,max}$.

A model of the sole interception was used to obtain values of effective precipitation (P_u) and potential transpiration ($E_{p,u}$) starting from total precipitation (P_t) and potential evaporation at the canopy level ($E_{p,i}$). Next the system without the interception was considered. Based on the assumption that when considering the long term water balance, variations of the storage can be neglected, the mean actual transpiration ($\overline{E_u}$) was obtained as follow:

$$(2.8) \quad \overline{E_u} = \overline{P_u} - \overline{Q_{obs}} \quad ,$$

where $\overline{P_u}$ is the mean effective precipitation over a period of nine years and $\overline{Q_{obs}}$ is the mean

observed discharge over a period of nine years. As a result, over the entire time series of 90 years, 10 different values of these statistics were obtained. Similarly, the mean potential transpiration ($\overline{E_{p,u}}$) was calculated every nine years. From the derived quantities, an estimation of the daily actual transpiration is obtained through the ratio of potential transpiration and long term mean potential transpiration. This allow to take into account seasonality, assuming that the variations around the mean are proportionally constant for potential and actual transpiration.

$$(2.9) \quad E_u(t) = \frac{E_{p,u}(t)}{\overline{E_{p,u}}} \quad .$$

As mentioned, in this work the long term statistics are assumed to change every 9 years.

For each day the water deficit was then calculated as the difference between actual evaporation and effective precipitation ($E_u - P_u$); the integration over consecutive positive values of the deficit gives the total cumulative water deficit for each dry spell, subsequently the maximum cumulative deficit for each year was taken. Equation 2.10 shows these steps for one year.

$$(2.10) \quad S_{R,1yr} = \max \int_{T_{in}}^{T_{en}} (E_u - P_u) dt \quad .$$

In equation 2.10, T_{in} and T_{en} are respectively initial and end time of a dry spell (i.e. times where the deficit equals zero). Figure 2.3 helps visualising equation 2.10 for the year 1995.

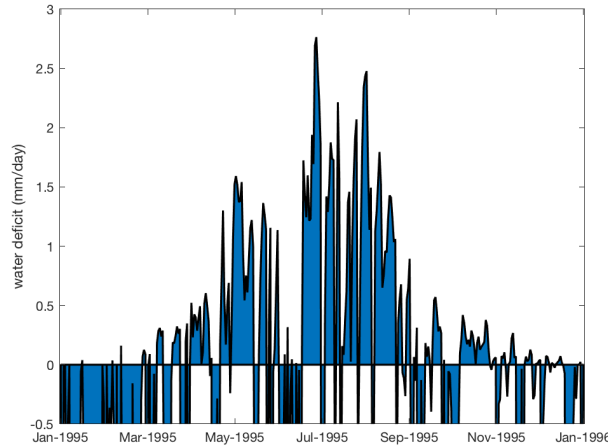


FIGURE 2.3. Daily water deficit (defined as $E_u - P_u$) for the year 1995. Positive values refer to day where precipitation was not enough to meet the water demand (transpiration) of vegetation. Each blue area represents the amount of water (mm) that the vegetation needs to take from the unsaturated reservoir to overcome the specific dry spell. $S_{R,1yr}$ for the year 1995 is the greatest of the blue areas in this figure.

Each blue area represents the cumulative water deficit of one dry spell. The greatest area is $S_{R,1yr}$ for the year 1995. Negative values of daily water deficit refer to days where effective precipitation was enough to meet the transpiration demand of vegetation.

According to the number of years used to calculate the long term statistics of the described procedure, the values of annual maximum water deficit ($S_{R,1yr}$) can vary significantly. Figure 2.4 shows the results obtained when evaluating the mean over 9, 15, 30 and 45 years.

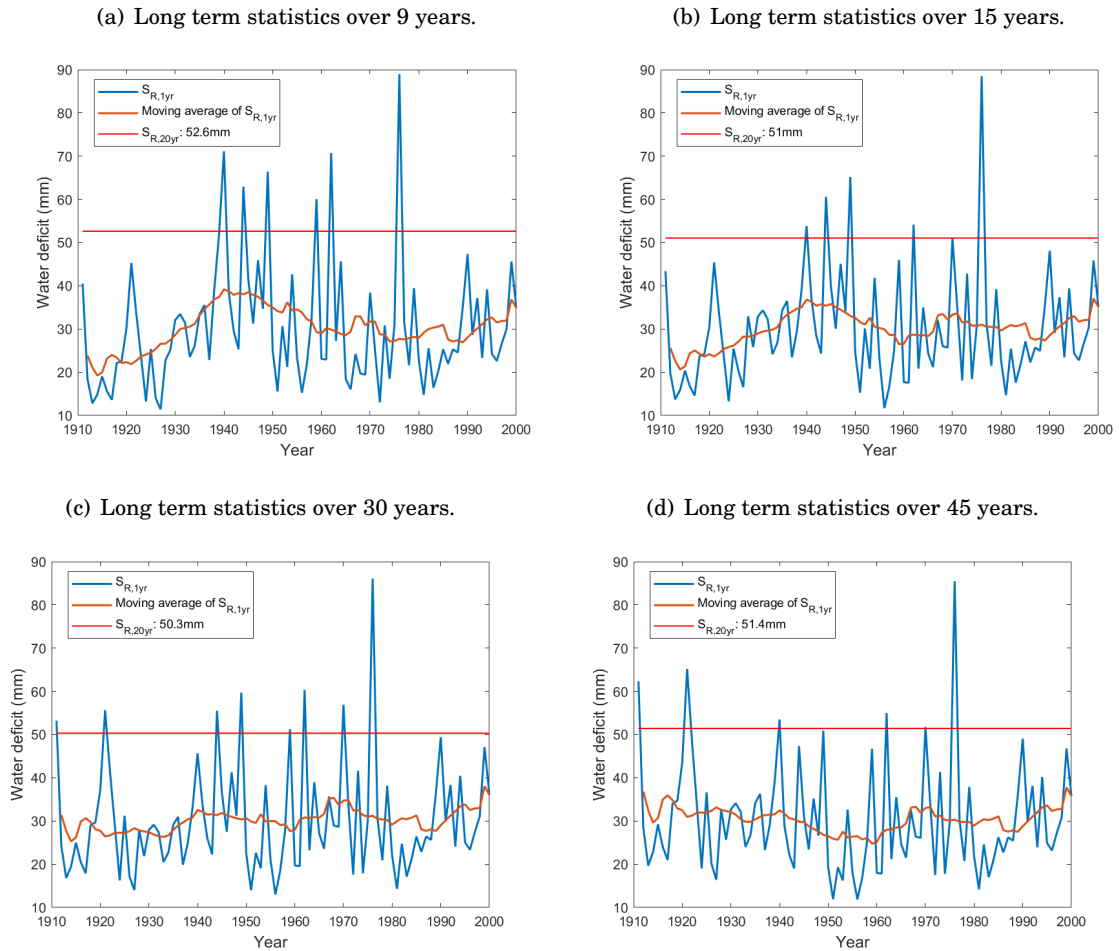


FIGURE 2.4. Results of the water-balance derived $S_{R,1yr}$ with mean values of potential transpiration, effective precipitation and observed discharge evaluated over different time intervals. The moving average (orange line) is calculated with a span of 20 values and help identifying a temporal trend of $S_{R,1yr}$, the water deficit with return period of 20 years ($S_{R,20yr}$, red line) is estimated using the Gumbel distribution.

The result obtained with long term statistics calculated over nine years was considered the most representative of the effective catchment situation. It allows to take into consideration relatively fast changes that might have occurred to the catchment and to the climate and still satisfy the assumption that $\frac{dS}{dt}$ is close to zero. Moreover, in figure 2.4(a) the trend highlighted

by the moving average appears to be strongly reflecting the anomaly observed by Ashagrie et al. (2006): underestimation of the discharge before 1935, overestimation of the discharge between 1935 and 1965 and a good fit after 1965; corresponding, in the figure, to lower values of $S_{R,1yr}$ before 1935 and higher values of $S_{R,1yr}$ between 1935 and 1965 compared to the values of $S_{R,1yr}$ obtained after 1965.

As mentioned before, a type I extreme value distribution (Gumbel) was used to fit the calculated values of $S_{R,1yr}$ and estimate droughts with a return period of 20 years (Nijzink et al., 2016). Although more than 20 years of data were available, the theoretical water deficit obtained with the extreme value distribution was preferred in respect of using the data directly. This decision helped giving consistency when changing the time interval from which deriving $S_{R,20yr}$ (experiment phase with time variability of $S_{u,max}$) and also reduced the weight of possible outliers in the data set.

First, all the 90 years were used to extract the quantity $S_{R,20yr}$, this was later assigned in the hydrological model as constant value of the variable $S_{u,max}$ (phase one of the second set of experiments). Figure 2.5 and figure 2.6 show the probability density function (PDF), cumulative distribution function (CDF) and inverse cumulative distribution function (ICDF) resulting from the data-fitting in the period 1911-2000.

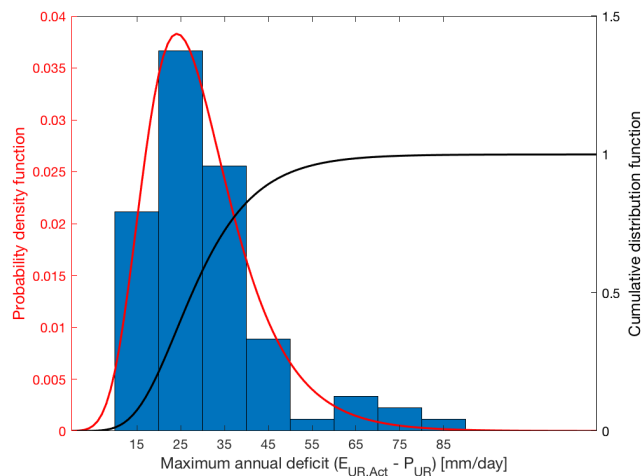


FIGURE 2.5. Probability density function (red line) and cumulative distribution function (black line) used to fit the annual maxima of water deficit from 1911 to 2000. The histogram, showing the counts of years for each range of water deficit, has been re-sized so that its total area sums to unity. The location parameter of the Gumbel distribution (μ) is 24.99 mm and the scale parameter (σ) is 8.97 mm

Although previous researches already identified periods of time with anomaly in the rainfall-runoff relationship, in this work the time windows have been tailored using figure 2.4(a): the mid century anomaly of the catchment behaviour goes from 1935 to 1964.

In a second moment, $S_{R,20yr}$ was calculated in each of the time intervals identified (1911-1934; 1935-1964; 1965-2000). The same method as described before was used: a Gumbel distribution was fitted to the annual maxima of water deficit for the selected time interval and, from it, the value of maximum water deficit with return period of 20 years was obtained.

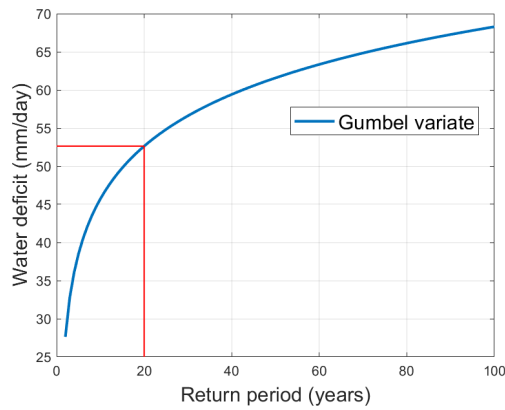


FIGURE 2.6. Inverse Cumulative Distribution Function of Gumbel distribution with parameters $\mu = 24.99mm$ and $\sigma = 8.97mm$. This function was directly used to obtain values of water deficit with a specific return period. $S_{R,20yr}$ was associated to the model parameter $S_{u,max}$, as suggested by Nijzink et al. (2016)

RESULTS

The outputs of the model used in this work are at daily resolution but, for a better representation and to maintain consistency with previous works (Fenicia et al., 2009; Ashagrie et al., 2006), a moving average with a time span of five years was applied to the mean annual discharge and the main considerations were made on the resulting hydrographs. It is important to recall that the objective function used in the calibration process compares the daily values of Q_{obs} and Q_{mod} , this means that the calibration process does not aim directly at correcting the observed mean anomalies but at obtaining better fit at daily resolution. As a result, a model setup with a better value of the objective function does not necessarily give a better fit of the mean annual discharge. The decision to keep a daily time step for the model run and model calibration was taken to use at best the available time resolution of the inputs.

The model outputs were analysed using some well known performance metrics. The Nash-Sutcliffe efficiency (NSE) is defined in equation 3.1 and was used to analyse the fit of the modelled discharge to the observed one. Similarly to the likelihood function, NSE evaluates the performance based on the squared distance of Q_{mod} from Q_{obs} . For each model set up, the NSE was evaluated on the daily data and on the mean annual values of the discharge (Q); the entire time series and the individual time windows were taken into account separately.

$$(3.1) \quad NSE = 1 - \frac{\sum_{i=T_0}^T (Q_{\text{mod},i} - Q_{\text{obs},i})^2}{\sum_{i=T_0}^T (Q_{\text{obs},i} - \overline{Q_{\text{obs}}})^2}$$

Table 3.1 shows the NSE for each model setup evaluated on the daily time resolution, while in table 3.3 the NSE is evaluated on annual mean values of Q . The same results of table 3.1 are graphically shown in figure 3.1.

Table 3.1: Nash-Sutcliffe efficiency (NSE) of daily discharge for different time intervals.

Model set up	1911-2000	1911-1934	1935-1964	1965-2000
Calibrated, constant $S_{u,max}$	0.8934	0.8912	0.8812	0.9026
Calibrated, varying $S_{u,max}$	0.8980	0.8965	0.8871	0.9060
WB derived, constant $S_{u,max}$	0.8553	0.8475	0.8480	0.8642
WB derived, varying $S_{u,max}$	0.8550	0.8386	0.8610	0.8595

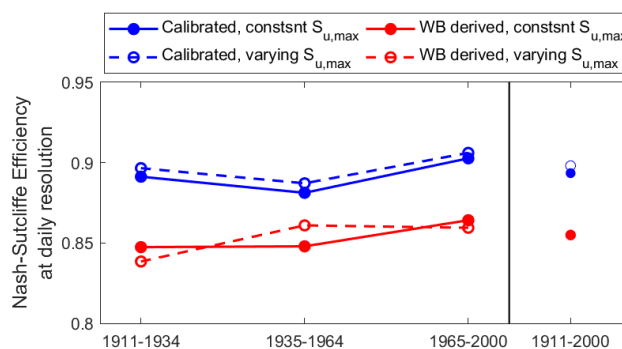


FIGURE 3.1. Graphic representation of Nash Sutcliffe Efficiency evaluated on daily discharge for the different setups at different time intervals.

When looking at table 3.1 it appears that the calibration of $S_{u,max}$ gives higher values of NSE. This result was predictable since having an extra calibration parameter always leads to a better (or equal) performance of the objective function. A more insightful way of reading table 3.1 would be to look separately to the two set of experiments (calibrated and WB derived $S_{u,max}$).

The first set of experiments (blue lines in figure 3.1) suggests that small improvements can be achieved on the daily discharge simulation giving time variability to the model parameters and without varying the potential transpiration: the greatest increase of the NSE index can be observed between 1935 and 1964 and NSE goes from 0.8812 to 0.8871.

When looking at the second set of experiments (red lines in figure 3.1) the overall performance remains almost the same with constant or time varying $S_{u,max}$; only the central time window shows an increase of the NSE (from 0.848 to 0.861). Although this shows a certain sensitivity of the model to the parameter, it looks like the WB derived values of $S_{u,max}$ worsen the performance of the model at daily resolution. Nevertheless, there are two important factors to consider. First, in the second set of experiments all the calibration parameters remained constant over the 90 years, even when varying $S_{u,max}$. Differently, in the first set of experiments, when considering time variability, all the parameters (except from L_e) were calibrated at every time interval. A second important element to be considered is the fact that, with the model equations used in this work, the unsaturated reservoir storage capacity might have a slight different role and physical meaning compared to the one given to the same parameter by Nijzink et al. (2016). The values of

$S_{u,\max}$ as resulting from calibration or climate data are listed in table 3.2.

Table 3.2: Used values of $S_{u,\max}$ (in mm).

Model set up	1911-1934	1935-1964	1965-2000
Calibrated, constant $S_{u,\max}$	164.5	164.5	164.5
Calibrated, varying $S_{u,\max}$	195.8	180.5	152.2
WB derived, constant $S_{u,\max}$	52.6	52.6	52.6
WB derived, varying $S_{u,\max}$	40.9	64.2	47.6

The differences between the derived and the calibrated values are greater than the one obtained by Nijzink et al. (2016) in other catchments, but on the same order of magnitude.

Since the WB derived value of $S_{u,\max}$ in the time invariant setup is lower than the calibrated one (52.6 mm compared to 164.5mm), any further reduction (as occurred from 1911 to 1934 and from 1965 to 2000) leads to lower values of NSE at daily resolution.

As visual example, the hydrograph of the largest flood event between 1911 and 2000 is presented in figure 3.2. It can be seen that time dependency of $S_{u,\max}$ gives little improvements to the fit; moreover, with the WB derived $S_{u,\max}$ the peak is underestimated. The shaded areas in figure 3.2 are the 95% confidence intervals for the output of the time invariant model runs; since calibration was done assuming a normal distribution of the error, these intervals correspond to $\pm 2\sigma$, where σ results from the calibration process as described in Chapter 2.3.1.

Although it is important for a model to capture peaks on daily time steps, especially if used for flood prediction, this work wants to analyse pluriannual anomalies.

Table 3.3: Nash-Sutcliffe efficiency (NSE) of annual averaged discharge for different time intervals.

Model set up	1911-2000	1911-1934	1935-1964	1965-2000
Calibrated, constant $S_{u,\max}$	0.6931	0.2571	0.3629	0.8761
Calibrated, varying $S_{u,\max}$	0.7138	0.3278	0.4115	0.8764
WB derived, constant $S_{u,\max}$	0.7168	0.3615	0.3721	0.8774
WB derived, varying $S_{u,\max}$	0.7996	0.5484	0.6810	0.8891

Interesting results are obtained when evaluating NSE on a moving average of the annual mean discharge (table 3.3). The models with a constant setup give their best fit during the last 35 years and perform very poorly during the anomaly time period. While this was already shown by Ashagrie et al. (2006) and Fenicia et al. (2009), here it is also possible to observe that when calibrating $S_{u,\max}$ on different time windows, the overall NSE increases only slightly (from 0.6931 to 0.7138) and remains insufficient ($NSE < 0.5$) from 1911 to 1964. Surprisingly, higher values of NSE are obtained by the model with WB derived $S_{u,\max}$ (with this setup the model has one calibration parameter less). First, looking at the constant setup, it can be seen that with a WB-derived value of $S_{u,\max}$ the NSE over 90 years is 0.7168 compared to $NSE = 0.6931$

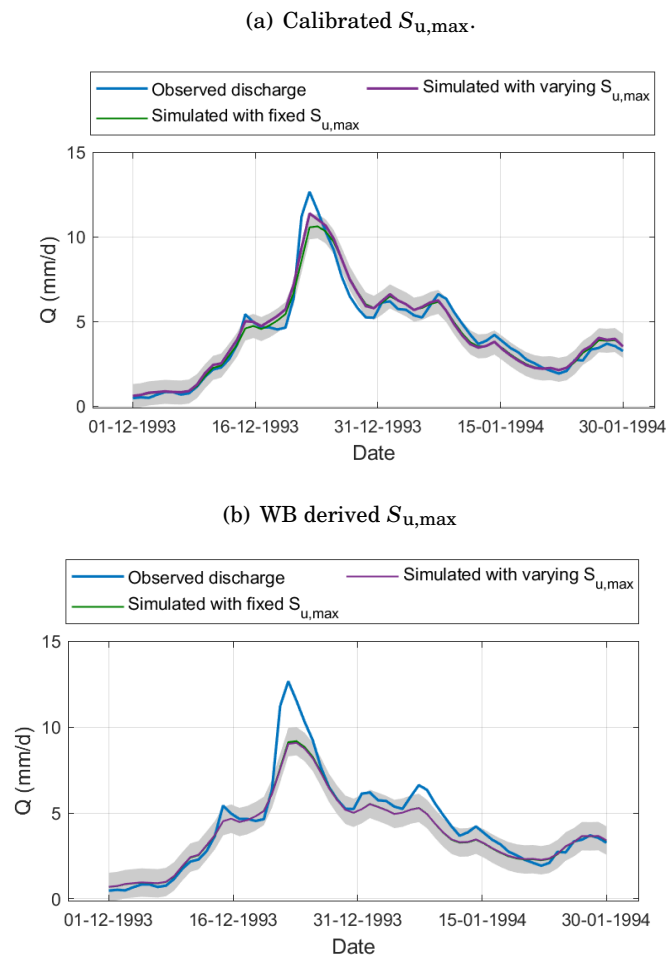


FIGURE 3.2. 3.2(a): hydrograph comparison of time invariant and time variant setup when using calibrated values of $S_{u,max}$. The shaded area shows the 95% confidence interval ($\pm 2\sigma$); the calibrated value ($\sigma=0.3552$ mm/d) refers to the time invariant setup. The selected time interval refers to the largest flood (December 1993) of the Meuse in the period 1911-2000. 3.2(b) is the equivalent graph for water balance derived $S_{u,max}$: $\sigma=0.4136$ mm/d.

for the model with the calibrated parameter. Secondly, the improvement given by adding time dependency to $S_{u,max}$ is greater for the WB derived case: the model performs sufficiently ($NSE > 0.5$) in all the time intervals and NSE goes from 0.7168 to 0.7996 when calculated over the 90 years.

Figure 3.3 summarises the information of table 3.3 and gives an overview of the model performances according to the Nash-Sutcliffe equation. The performance of the two models is similar with constant parametrization (solid lines), but only when $S_{u,max}$ is derived from the water balance, time variability significantly improves the efficiency (red dashed line).

For a better understanding of the results and to endorse what stated above, the Nash-Sutcliffe

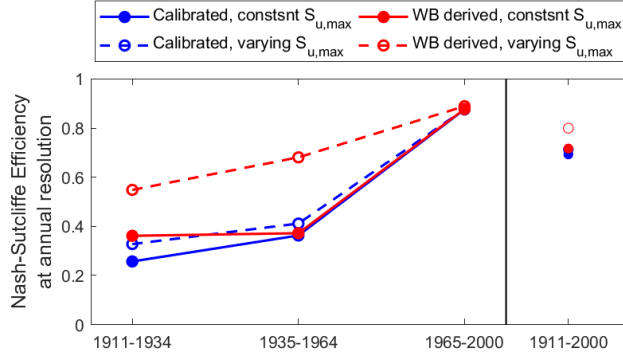


FIGURE 3.3. Graphic representation of Nash Sutcliffe Efficiency evaluated on annual mean discharge for the different setups at different time intervals.

efficiency of the log of the flow NSE_{\log} , the volumetric bias VE (Criss and Winston, 2008) and the coefficient of determination R^2 (Krause et al., 2005) were also calculated and used to compare the different model setups. Table 3.4 and table 3.5 list these performance metrics computed over 90 years for a daily data set and for the averaged data set.

Table 3.4: Performance metrics evaluated over the period 1911-2000 from daily data.

Model set up	NSE_{\log}	VE	R^2
Calibrated, constant $S_{u,max}$	0.8563	0.9790	0.8938
Calibrated, varying $S_{u,max}$	0.8093	0.9813	0.8984
WB derived, constant $S_{u,max}$	0.8160	0.9848	0.8561
WB derived, varying $S_{u,max}$	0.8153	0.9851	0.8559

Table 3.5: Performance metrics evaluated over the period 1911-2000 from annual averaged data.

Model set up	NSE_{\log}	VE	R^2
Calibrated, constant $S_{u,max}$	0.6975	0.9813	0.7217
Calibrated, varying $S_{u,max}$	0.7191	0.9827	0.7362
WB derived, constant $S_{u,max}$	0.7285	0.9894	0.7243
WB derived, varying $S_{u,max}$	0.8049	0.9898	0.8117

The definition of VE and R^2 are given respectively in equation 3.2 and equation 3.3

$$(3.2) \quad VE = 1 - \frac{\sum_{i=T_0}^T |Q_{obs,i} - Q_{mod,i}|}{\sum_{i=T_0}^T Q_{obs,i}}$$

$$(3.3) \quad R^2 = \left(\frac{\sum_{i=T_0}^T (Q_{\text{obs},i} - \overline{Q_{\text{obs}}})(Q_{\text{mod},i} - \overline{Q_{\text{mod}}})}{\sqrt{\sum_{i=T_0}^T (Q_{\text{obs},i} - \overline{Q_{\text{obs}}})^2} \sqrt{\sum_{i=T_0}^T (Q_{\text{mod},i} - \overline{Q_{\text{mod}}})^2}} \right)^2$$

All the performance metrics used are defined in the interval [0 1] and the maximum value correspond to the best performance. The volumetric bias gives information on the volume of water missing for a perfect closure of the water balance, while the coefficient of determination estimates the combined dispersion against the single dispersion of the observed and modelled discharge (Krause et al., 2005). Since only the dispersion is quantified by this coefficient, a model with systematic overestimation (or underestimation) of the discharge will still deliver a good value of R^2 . Multiple performance metrics should always be used to validate a model.

It is interesting to notice that the VE increases when evaluated over mean values of Q ; differently, all the other performance metrics experience a decrease compared to their corresponding value on daily time steps.

3.1 Hydrographs

It was mentioned already that when calibrating $S_{u,\text{max}}$ the number of calibration parameters increases and this is necessarily reflected on a better performance of the model evaluated at daily time steps. When analysing the annual mean discharge this effect is levelled off as indicated by the performance metrics presented above and as it can be seen in figure 3.4.

Using a constant value of $S_{u,\text{max}}$ the anomalies observed by Ashagrie et al. (2006) can be reproduced by the FLEX model used in this work for both set of experiments (calibrated and WB derived $S_{u,\text{max}}$). The differences observed in figure 3.4 are small even if the two runs use very different values of $S_{u,\text{max}}$, this means that the other parameters are largely able to compensate for this change. The equifinality of this conceptual model, already detected by Fenicia et al. (2009), poses many questions on the actual meaning of the parameters used. One of the reason to use a water balance derived UR storage capacity is to reduce the number of calibrated parameters and so the equifinality of the model. Furthermore, an increasing body of evidence shows that this method well describes the physical role of $S_{u,\text{max}}$.

Figure 3.5 presents the hydrographs obtained from the first experiment setup: when calibrating the root zone storage capacity, the addition of time dependency to the latter gives a minimal improvement to the mean streamflow simulation. One possible explanation is that the process causing the discharge anomaly is not included or independently represented by the model. Perhaps certain features like forest age (as proposed by Fenicia et al. (2009)) are actually responsible of a direct alteration of the transpiration fluxes. Another possibility is that the implementation of the perceptual and conceptual model should be revised because one or more of the parameters accounts for multiple catchment characteristics, resulting in the impossibility

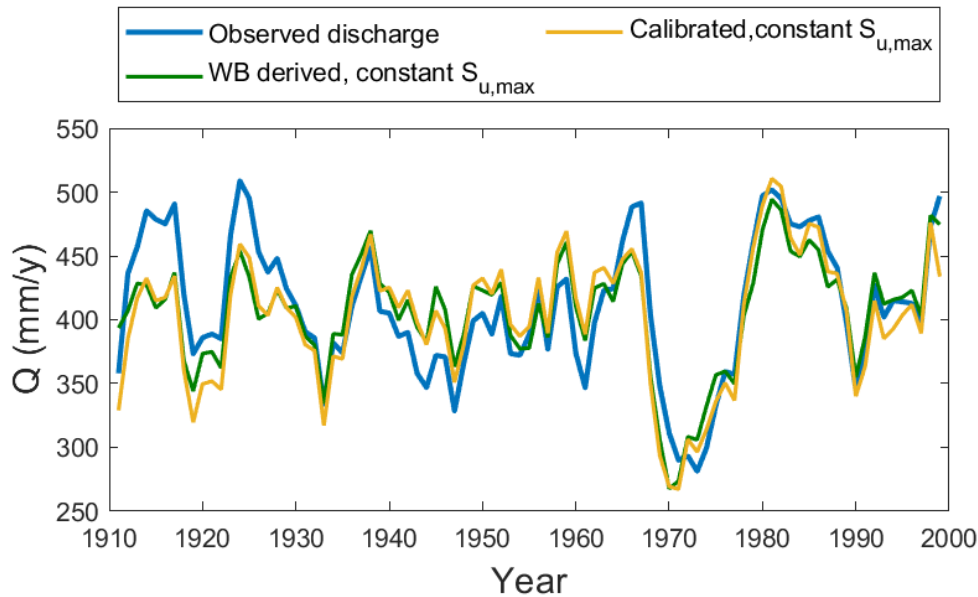


FIGURE 3.4. Hydrograph from constant $S_{u,max}$ in the case of calibrated and water balance derived $S_{u,max}$.

of mimicking temporal variability of the rainfall-runoff relationship. In this work an attempt to constrain the model parameter representing root-zone storage capacity was done using the method proposed by Gao et al. (2014) and explained in Chapter 2. Figure 3.6 shows the results obtained with this second setup.

It can be seen that, giving time dependency to $S_{u,max}$ when calculated from climate data, delivers a a better fit to the average discharge. The correction does not fully explains the anomaly, but demonstrates that the variability of the transpiration rate with stand age obtained by Fenicia et al. (2009) was an overestimation and was accounting for time variability of other catchment characteristics (i.e. root-zone storage capacity). Equifinality is reduced with this second setup and model sensitivity to $S_{u,max}$ is increased since, relatively small changes of $S_{u,max}$ produce an appreciable variation of the model output and the number of calibrated parameters is reduced.

As mentioned before, it is interesting to notice how the comparison between the different experiments depends on the time scale at which the outputs are analysed. This fact is also reflected on the model error as output of the calibration process at daily time scale. When averaging the data to annual mean and performing a moving average, the error distribution is affected and it is not possible to assume it to be Gaussian. For this reason the 95% confidence interval was empirically obtained calculating the 2.5th and 97.5th percentile from 500 possible realisation of the modelled discharge.

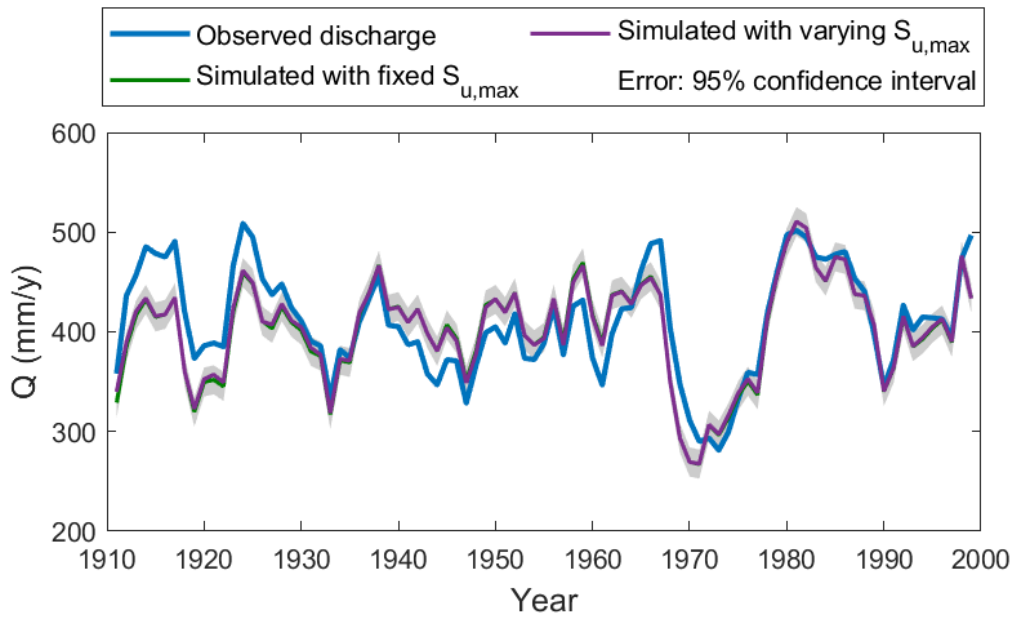


FIGURE 3.5. Hydrograph comparison of time invariant and time variant setup when using calibrated values of $S_{u,max}$. The calibrated confidence interval, shown as shaded area, refers to the time invariant setup.

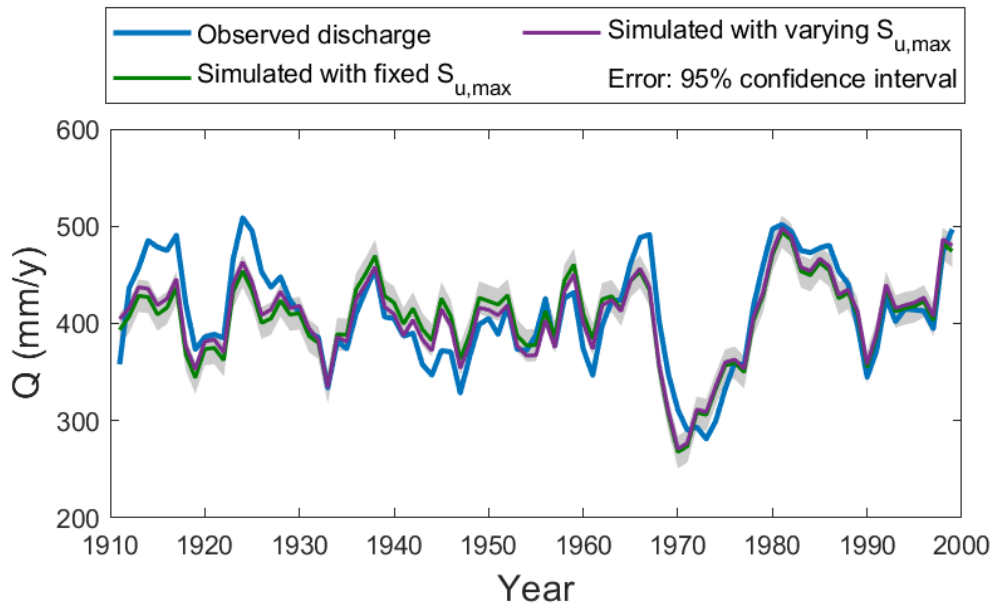


FIGURE 3.6. Hydrograph comparison of time invariant and time variant setup when using WB derived $S_{u,max}$. The calibrated confidence interval, shown as shaded area, refers to the time invariant setup.

500 randomly generated hydrographs with daily time values of Q were obtained adding to the simulated discharge a random error normally distributed: $N(0, \sigma)$; where σ was obtained in the calibration phase. To each of the 500 hydrographs the annual mean and the moving average was performed, then the desired percentile was obtained each year from the 500 values of Q .

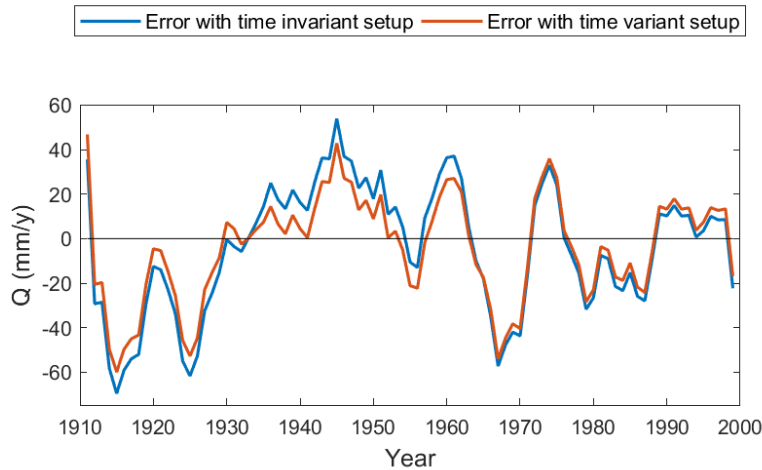


FIGURE 3.7. Deviation from the observed discharge ($Q_{\text{mod}} - Q_{\text{obs}}$) in the case of WB derived $S_{u,\text{max}}$. Blue line for the model with a constant value of the parameter and orange line for the model with varying $S_{u,\text{max}}$.

Figure 3.7 shows another effective representation of the improvements obtained with time dynamic and WB derived $S_{u,\text{max}}$: the actual deviation of the modelled discharge from the observations. The mean overestimation between 1935 and 1964 and the underestimation before 1935 are clearly visible and a time dependent $S_{u,\text{max}}$ delivers a slight improvement.

Results can also be presented through scatter plots of the modelled mean annual discharge versus the observed mean annual discharge (see figure 3.8). When data points are aligned on the bisector the modelled discharge is equal to the observed discharge. To obtain figure 3.8 the moving average was not applied to the mean discharges. As mentioned before, it can be seen that when calibrating $S_{u,\text{max}}$, time variability of the model parameters gives a minimal improvement (from figure 3.8(a) to figure 3.8(c)). Differently, with a WB derived $S_{u,\text{max}}$ the green points, representing years from 1935 to 1964, get noticeably closer to the bisector when adding time dependency (from figure 3.8(b) to figure 3.8(d)). This means that, during the anomaly period, mean annual modelled discharges are partly corrected by changing the value of $S_{u,\text{max}}$. From figure 3.8 it is also possible to notice that the regression lines in the case of calibrated $S_{u,\text{max}}$ are always parallel to the bisector, while they show a worsening of the fit for high discharges in the case of WB derived $S_{u,\text{max}}$. This means that the first set of experiments gives a constant error in each of the time windows, while the error in reproducing mean annual discharge of the second set of experiments increases for greater values of Q .

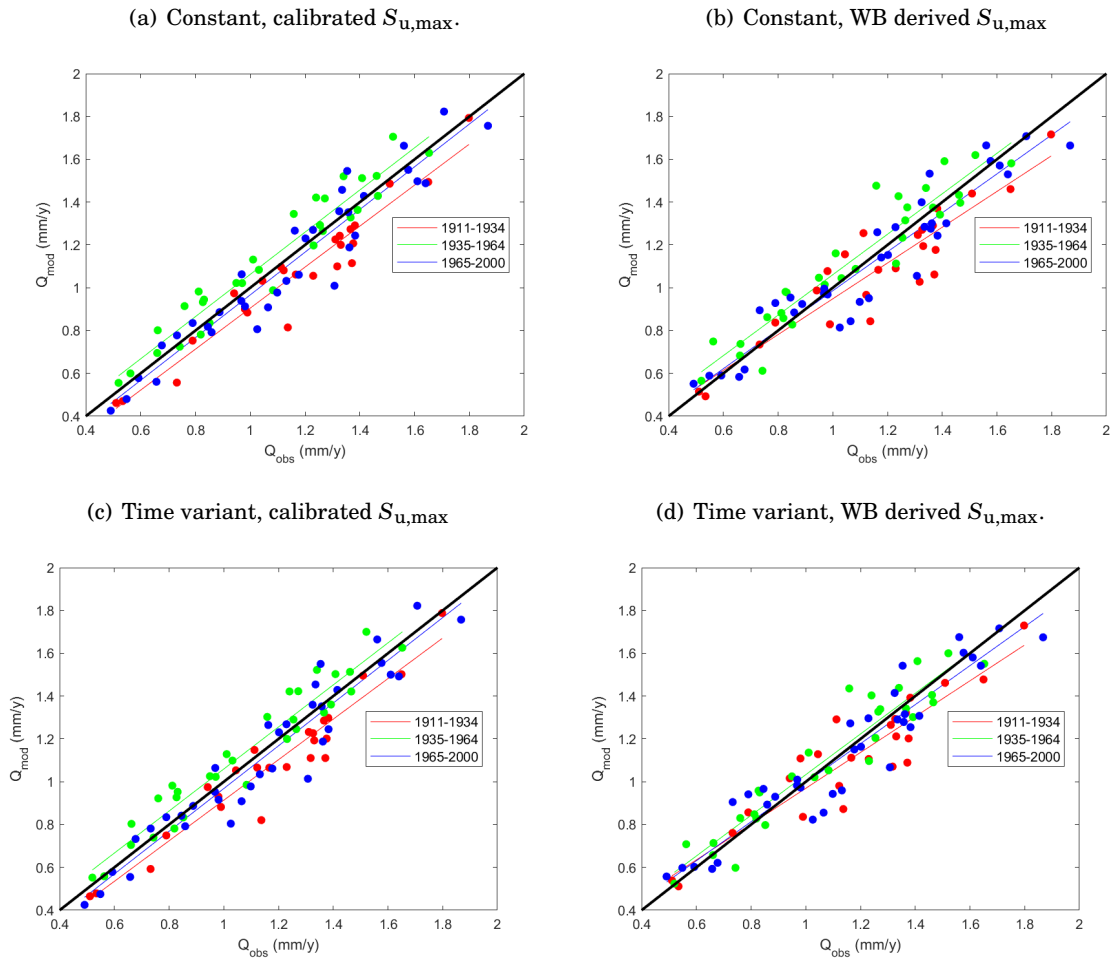


FIGURE 3.8. Scatter plots of the modelled and observed mean annual discharges (mm/year); red dots refer to the years from 1911 to 1934, green dots to the years 1935 to 1964 and blue dots to the years 1965 to 2000. Each sub-figure corresponds to one of the four experiments: 3.8(a) for time invariant setup and calibrated $S_{u,\max}$, 3.8(b) for time invariant setup and WB derived $S_{u,\max}$, 3.8(c) for time variant setup and calibrated $S_{u,\max}$, 3.8(d) for time variant setup and WB derived $S_{u,\max}$.

3.2 Actual transpiration

Assuming that the model ensures a closure of the water balance, the model performance can be evaluated, indifferently, on the accuracy of reproducing the observed discharge (as done in the previous section) or, on the accuracy of reproducing the actual transpiration. Logically, under this assumption, when the discharge is overestimated, the actual transpiration is underestimated by the model.

Although the volumetric bias (VE), presented at the beginning of Chapter 3, is always greater than 0.95, and so the assumption of a reasonable closure of the water balance can be done, an analysis of the actual transpiration can give further insights on the experiments' results.

Figure 3.9 shows a time series of the actual transpiration as modelled when calibrating $S_{u,max}$ (orange and yellow lines) and the reference actual transpiration obtained from equation 2.9 (blue line).

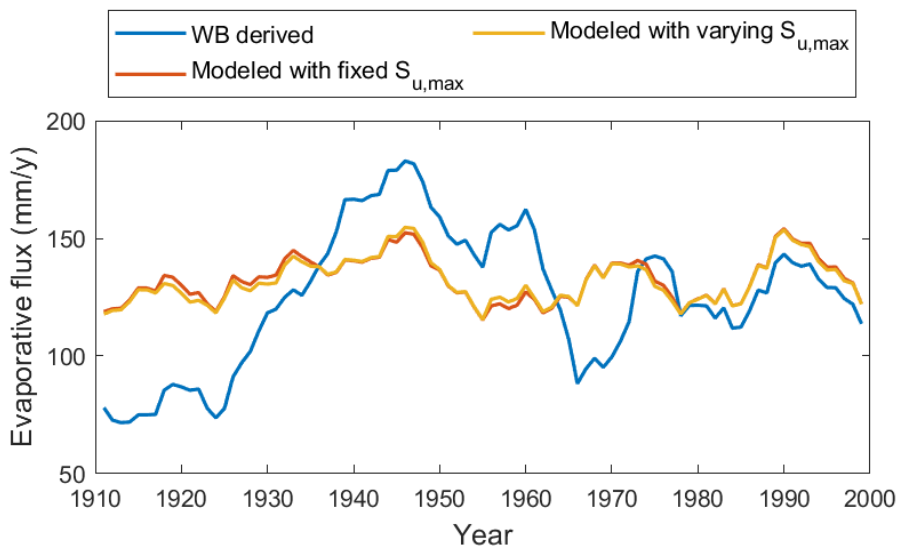


FIGURE 3.9. Modelled actual transpiration of time invariant and time variant setup when using calibrated values of $S_{u,max}$ compared to the actual transpiration calculated from long term statistics.

Once more, in figure 3.9 the time varying $S_{u,max}$ (yellow line) only gives a small improvement to the fit compared to the improvement from the orange line to the yellow line observed in figure 3.10 (actual transpiration modelled with WB derived $S_{u,max}$).

When looking at the short time variability of actual transpiration modelled with a calibrated $S_{u,max}$ (figure 3.9) and of actual transpiration modelled with a WB derived $S_{u,max}$ (figure 3.10), some interesting considerations can be done. Even if values are distant from the observed ones, the orange and the yellow lines in figure 3.9 reproduce the short time trends of the blue line:

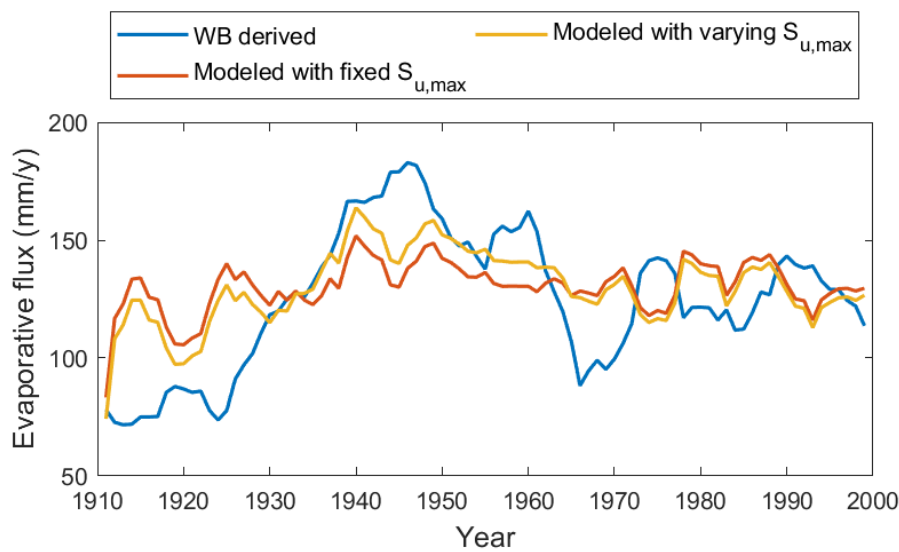


FIGURE 3.10. Modelled actual transpiration of time invariant and time variant setup when using WB derived values of $S_{u,max}$ compared to the actual transpiration calculated from long term statistics.

if the blue line decrease from one year to the other, the modelled transpiration also shows a decreasing trend. Instead, in figure 3.10 the short time scale variability of the modelled actual transpiration behaves oppositely to the one derived a priori (blue line). This can be seen looking at the first 20 years of the time series: the years around 1920 show a local maximum of the blue curve, while for the same years, the orange and the yellow lines show a local minimum.

A final representation of the results is shown in figure 3.11. Here, together with the actual transpiration obtained from equation 2.9 (blue line), the actual transpiration obtained as output of three time varying models is plotted. The green line is obtained reproducing the results of Fencia et al. (2009): calibrating the parameter L_e in different time windows. The purple line is given by the model with time varying and WB derived $S_{u,max}$; the orange line is given by the model with time varying and calibrated $S_{u,max}$.

In this case the green line is used as benchmark. Apart from the short time scale variability, the purple line gives a reasonable inter-annual trend of actual transpiration: higher values in the central decades of the century and lower values in the first decades of the century. Differently, the orange line seems to be missing this trend and remains horizontal over the 90 years of simulation.

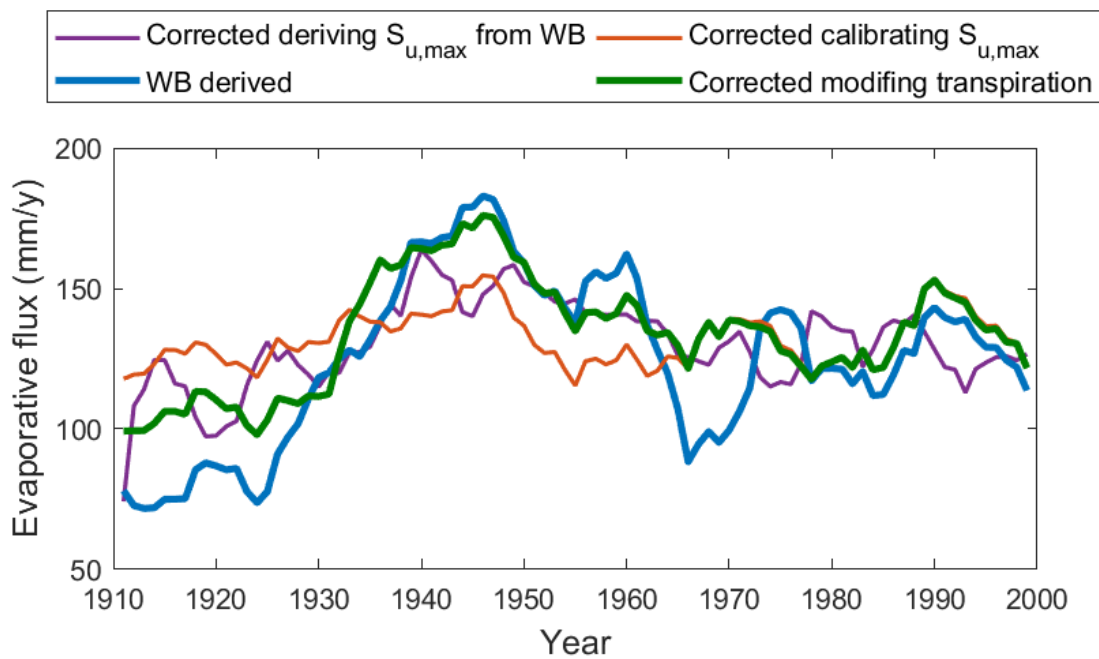


FIGURE 3.11. Actual transpiration calculated a priori and actual transpiration as output of time variant models: $S_{u,max}$ from climate data (purple line), calibrated $S_{u,max}$ (orange line) and time variant transpiration coefficient (green line).

DISCUSSION AND REMARKS

In this chapter some important aspects that may have significantly affected the results of the study are discussed.

First, it is important to stress one more time the importance of the time scale at which the model is calibrated and then evaluated. Later studies might want to consider an objective function that uses mean annual values of discharge instead of daily values. Another aspect to focus on, is the physical role of the parameter $S_{u,max}$. For instance, it is often hard to understand if a conceptual model uses it as the maximum amount of water that the soil can store or if it considers $S_{u,max}$ as the maximum amount of water available for vegetation during dry periods. In this work the method proposed by Nijzink et al. (2016) was used to calculate the root-zone storage capacity, but the constitutive function for runoff generation was different from the one used in the mentioned research. It is arguable that, according to the conceptualisation of the perceptual model, the parameter $S_{u,max}$ considers slightly different catchment properties. Different conceptual models should be used in later studies to investigate the reliability of a water balance derived $S_{u,max}$ in the Meuse river basin. Furthermore, the consequences of the assumption that long-term statistics of equation 2.8 are taken over 9 years should be better analysed.

The way time variability is added to the model is also a sensitive aspect for the realism of the experiments: here it was assumed that on the years selected as limits of the anomaly period (1934 and 1965) the root-zone storage capacity "jumped" from one value to the other without any gradual transition. Nijzink et al. (2016) showed that in other catchments the recovery period of roots after deforestation goes from 5 to 13 years, so it is reasonable to assume that a transition period of at least 5 years should be considered before and after the anomaly discussed in the present work.

A further remark on the approach used concerns the model validation. A more structured

validation phase should be planned; in this work few performance metrics and an analysis of the actual transpiration fluxes were used to validate the results, but a comparison with neighbouring catchments could be performed, as done by Min Tu (2006).

At last, an assessment of the added value of the reduction in the number of parameters would give more information to compare the two experiment setups of this work.

CONCLUSIONS

In the present work, time variability of the root-zone storage capacity ($S_{u,max}$) was added to a semi-distributed conceptual model of the Meuse river basin in order to explain systematic mean annual anomalies of the river discharge. The parameter $S_{u,max}$ was obtained, in a first experiment setup, by calibrating it in different time windows (1911-1934; 1935-1964; 1965;2000); in a second experiment setup, $S_{u,max}$ was derived for each of the three time windows from climate data. The results showed that, when derived from climate data, time variability of the root-zone storage capacity delivers a noticeable, but not absolute, improvement of the modelled annual mean discharge.

It is clear that the root-zone storage capacity is not the only catchment characteristic which changed over the analysed century because the anomaly is not entirely corrected with the approach used in this work. Nevertheless, it can be stated that the explanation to the anomaly given by Fenicia et al. (2009) overestimated the dependency of transpiration to stand age. With the reduction of the number of calibration parameters and the constrain of $S_{u,max}$ to a rigorous physical interpretation, this work also tackles the problem of equifinality and moves towards a better understanding of catchment properties.

Future studies should investigate which other processes were responsible for the change in the rainfall-runoff behaviour of the Meuse during the past century; perhaps by analysing the links between root-zone storage capacity and forest transpiration rate.

DETAILS OF THE HYDROLOGICAL MODEL

This appendix synthetically reports the equations and parameters used when implementing the model structure.

A.1 List of equations

Table A.1 describes all the constitutive functions relating storages and fluxes.

$E_{p,i}$ (potential evaporation from the interception) and E_{Penm} (potential evaporation from UR according to Penman-Monteith equation) are obtained from the Penman-Monteith equation (eq. A.1)

$$(A.1) \quad E_p = \frac{1}{\lambda \rho_w} \frac{s R_n + c_p \rho_a (e_a - e_d) / r_a}{s + \gamma (1 + r_c / r_a)}.$$

The variables used in equation A.1 are described in table A.2.

The Lag function, or transfer function, which relates P_{Π} to P_f is defined with a convolution integral as follow:

$$(A.2) \quad (P_f * LW_f)(t) = \int_0^t P_f(\tau) LW_f(t - \tau) d\tau.$$

This means that after shifting the response distribution and assigning the weights to the new precipitation input (P_f), the value corresponding to $t = N_{lagf}$ is given as output of the transfer function. In this case the function LW_f has a triangular shape.

Table A.1: Model equations

Equation	Definition
$\frac{dS_i}{dt} = P_t - E_i - P_u$	Interception reservoir storage balance
$\frac{dS_u}{dt} = P_u - E_u - Q_q - Q_u$	Unsaturated reservoir storage balance
$\frac{dS_f}{dt} = P_{fl} - Q_f$	Fast reservoir storage balance
$\frac{dS_s}{dt} = P_s - Q_s$	Slow reservoir storage balance
$\overline{S}_i = \frac{S_i}{S_{i,\max}}$	Interception reservoir fullness rate
$\overline{S}_u = \frac{S_u}{S_{u,\max}}$	Unsaturated reservoir fullness rate
$E_a = E_i + E_u$	Total actual evaporation
$Q_t = Q_f + Q_s$	Total discharge
$P_s = Q_u + Q_p$	Inflow to SR
$Q_p = DQ_q$	Preferential recharge
$P_f = Q_q - Q_p$	Inflow to the lag function
$P_{fl} = (P_f * LW_f)(t)$	Inflow to FR
$LW_f = \begin{cases} 2t/Nlagf, & t < Nlagf \\ 0, & t > Nlagf \end{cases}$	Weights of triangular lag function
$P_u = P_t f(\overline{S}_i \alpha) = P_t \overline{S}_i^\alpha$	Effective precipitation
$E_i = E_{p,i} f(\overline{S}_i m) = E_{p,i} \overline{S}_i^{\frac{1+m}{S_i-m}}$	Actual evaporation from IR
$Q_q = P_u f(\overline{S}_u \beta) = P_u \frac{C_r - C_{r,\min}}{C_{r,\max} - C_{r,\min}}$	Runoff
$C_r = \frac{1}{1 + \exp\left(\frac{-\overline{S}_u + 1/2}{\beta}\right)}$	Runoff coefficient
$Q_u = f(\overline{S}_u k_b) = k_b \overline{S}_u$	Percolation from UR
$E_u = E_{p,u} f(\overline{S}_u m, L_e) = E_{p,u} L_e \overline{S}_u^{\frac{1+m}{S_u-m}}$	Actual transpiration from UR
$E_{p,u} = \min(E_{Pen}, E_{p,i} - E_i)$	Potential transpiration
$Q_s = f(S_s K_s) = \frac{S_s}{K_s}$	Slow discharge
$Q_f = f(S_f K_f) = \frac{S_f}{K_f}$	Fast discharge

Table A.2: Description of the Penman-Monteith equation

Parameter	Definition	Units
E_p	Potential evaporation	m/s
λ	Latent heat coefficient	J/kg
ρ_w	Density of water	kg/m ³
R_n	Net radiation	W/m ²
s	Slope of the temperature-saturation vapour pressure curve	kPa/K
c_p	Specific heat of air at constant pressure	J/(kg K)
ρ_a	Density of air	kg/m ³
e_d	Actual vapour pressure of air	kPa
e_a	Saturation vapour pressure for the air temperature	kPa
γ	Psychrometric constant	kPa/K
r_a	Aerodynamic resistance	s/m
r_c	surface resistance	s/m

A.2 Model parameters

The hydrological model used in this work has 11 parameters and one parameter for the error model (σ), three of the parameter were never calibrated but taken from the literature. For example, the parameters α and m are introduced to smooth discontinuity of constitutive functions in the interception model; these functions were not continuous in the model used by Fenicia et al. (2009).

Table A.3: Model parameters

Parameter	Definition	Range	Units
β	Shape parameter of runoff generation	0.05-0.5	-
K_b	Percolation rate	0-0.9	mm/d
m	Shape parameter Evaporation smoothing	0.01	-
α	Shape parameter of release from interception	5	-
D	Runoff partition coefficient	0-0.6	-
K_f	FR time scale	2-10	d
K_s	SR time scale	10-100	d
N_{lagf}	Lag-time of FR transfer function	1-4	d
C_i	Interception factor	2 (Fenicia et al., 2009)	-
L_e	Correction factor for Transpiration	0.2-1.8	-
$S_{u,max}$	*Maximum UR storage	20-500	mm
σ	Error	0.02-2	mm/d

α and m are not calibrated but are listed with the parameters because a variation in their values can affect the model performance; moreover, they have not a direct physical meaning but are used to smooth the response function of the interception reservoir and of the evaporation to the state of the corresponding reservoir. Similarly, the interception factor (C_i) is kept constant to the value calibrated by Fenicia et al. (2009). This allow to run a model of the solely interception reservoir without the need to calibrate its parameters.

The parameter $S_{u,max}$ is marked with an asterisk (*) because it is calibrated in the given range only for the first of the two sets of experiments, otherwise its value is obtained from climate data as described in Chapter 2.4.1.

At last, the parameter L_e was kept constant over the 90 years of simulation for each of the experiments.

BIBLIOGRAPHY

- Ashagrie, A. G., De Laat, P. J. M., De Wit, M. J. M., Tu, M., and Uhlenbrook, S. (2006).
Detecting the influence of land use changes
Detecting the influence of land use changes on
Floods in the Meuse River Basin – the predictive power of a ninety-year rainfall-runoff relation
Detecting the influence of land use changes.
HESSD Hydrol. Earth Syst. Sci. Discuss, 3(3):529–559.
- Bouaziz, L. and Hrachowitz, M. (2017).
What controls the very quick runoff response in the Meuse basin?
Geophysical Research Abstracts EGU General Assembly Laurène Bouaziz Jaap Schellekens Laurene.Bouaziz@deltares.nl Water Resources Section, 191(2211212):2017–14266.
- Clark, M. P. and Kavetski, D. (2010).
Ancient numerical daemons of conceptual hydrological modeling: 1. Fidelity and efficiency of
time stepping schemes.
Water Resources Research.
- Criss, R. E. and Winston, W. E. (2008).
Do nash values have value? discussion and alternate proposals.
Hydrological Processes, 22(14):2723–2725.
- Dale, V. H. V. H. (1997).
The Relationship Between Land-Use Change and Climate Change.
Ecological Applications, 7(3):753–769.
- de Boer, T. (2017).
Added value of distribution in rainfall-runoff models for the Meuse basin.
- de Boer-Euser, T., McMillan, H. K., Hrachowitz, M., Winsemius, H. C., and Savenije, H. H. G.
(2016).
Influence of soil and climate on root zone storage capacity.
Water Resources Research, 52(3):2009–2024.
- De Roo, A., Odijk, M., Schmuck, G., Koster, E., and Lucieer, A. (2001).
Assessing the effects of land use changes on floods in the meuse and oder catchment.

BIBLIOGRAPHY

- Physics and Chemistry of the Earth, Part B: Hydrology, Oceans and Atmosphere*, 26(7-8):593–599.
- Duan, Q., Sorooshian, S., and Gupta, V. (1992).
Effective and efficient global optimization for conceptual rainfall-runoff models.
Water Resources Research, 28(4):1015–1031.
- Duan, Q. Y., Gupta, V. K., and Sorooshian, S. (1993).
Shuffled complex evolution approach for effective and efficient global minimization.
Journal of Optimization Theory and Applications, 76(3):501–521.
- EEA (2001).
Sustainable water use in Europe. Part 3: Extreme hydrological events: floods and droughts.
Technical Report 21, European Environmental Agency (EEA), Copenhagen.
- Fenicia, F., Kavetski, D., and Savenije, H. H. G. (2011).
Elements of a flexible approach for conceptual hydrological modeling: 1. Motivation and theoretical development.
Water Resources Research, 47(11).
- Fenicia, F., Kavetski, D., Savenije, H. H. G., Clark, M. P., Schoups, G., Pfister, L., and Freer, J. (2014).
Catchment properties, function, and conceptual model representation: is there a correspondence?
Hydrological Processes, 28(4):2451–2467.
- Fenicia, F., Savenije, H. H., and Avdeeva, Y. (2009).
Anomaly in the rainfall-runoff behaviour of the Meuse catchment. Climate, land-use, or land-use management?
Hydrology and Earth System Sciences, 13(9):1727–1737.
- Fenicia, F., Savenije, H. H. G., Matgen, P., and Pfister, L. (2007).
A comparison of alternative multiobjective calibration strategies for hydrological modeling.
Water Resources Research, 43(3).
- Gao, H., Hrachowitz, M., Schymanski, S. J., Fenicia, F., Sriwongsitanon, N., and Savenije, H. H. G. (2014).
Climate controls how ecosystems size the root zone storage capacity at catchment scale.
Geophysical Research Letters, 41(22):7916–7923.
- Gumbel, E. J. (1941).
The return period of flood flows.
Ann. Math. Statist., 12(2):163–190.

- Kavetski, D. and Clark, M. P. (2010).
Ancient numerical daemons of conceptual hydrological modeling: 2. impact of time stepping schemes on model analysis and prediction.
Water Resources Research, 46(10).
- Krause, P., Boyle, D. P., and Bäse, F. (2005).
Comparison of different efficiency criteria for hydrological model assessment.
Advances in Geosciences, 5:89–97.
- Kwadijk, J. and Rotmans, J. (1995).
The impact of climate change on the river rhine: A scenario study.
Climatic Change, 30(4):397–425.
- Min Tu, M. (2006).
Assessment of the effects of climate variability and land use changes on the hydrology of the Meuse River Basin.
PhD thesis, Vrije Universiteit Amsterdam.
Naam instelling promotie: VU Vrije Universiteit Naam instelling onderzoek: VU Vrije Universiteit.
- Nienhuis, P. H. (2008).
Environmental history of the rhine-meuse delta: An ecological story on evolving human-environmental relations coping with climate change and sea-level rise.
Springer Netherlands, Dordrecht.
- Nijzink, R., Hutton, C., Pechlivanidis, I., Capell, R., Arheimer, B., Freer, J., Han, D., Wagener, T., McGuire, K., Savenije, H., and Hrachowitz, M. (2016).
The evolution of root-zone moisture capacities after deforestation: a step towards hydrological predictions under change?
Hydrol. Earth Syst. Sci, 20:4775–4799.
- Peel, M. C. and Blöschl, G. (2011).
Hydrological modelling in a changing world.
Progress in Physical Geography, 35(2):249–261.
- Pfister, L., Kwadijk, J., Musy, A., Bronstert, A., and Hoffmann, L. (2004).
Climate change, land use change and runoff prediction in the Rhine-Meuse basins.
River Research and Applications, 20(3):229–241.
- Tu, M., Hall, M., De Laat, P., and De Wit, M. (2004).
Detection of long-term changes in precipitation and discharge in the meuse basin.
IAHS-AISH Publication, pages 169–177.

BIBLIOGRAPHY

Tu, M., Hall, M. J., de Laat, P. J., and de Wit, M. J. (2005).

Extreme floods in the Meuse river over the past century: aggravated by land-use changes?
Physics and Chemistry of the Earth, Parts A/B/C, 30(4-5):267–276.

Ward, P. J., Renssen, H., Aerts, J. C. J. H., van Balen, R. T., and Vandenberghe, J. (2008).

Strong increases in flood frequency and discharge of the river Meuse over the late holocene: impacts of long-term anthropogenic land use change and climate variability.
Hydrology and Earth System Sciences, 12(1):159–175.

Wit, M., Warmerdam, P.M.M., T., Orfs, P., Uijlenhoet, R., Cheymol, a., Deursen, W., Walsum, P., Ververs, M., Kwadijk, J., and Buiteveld, H. (2001).

Effect of climate change on the hydrology of the river Meuse.
6(8):103–130.